Topological phonons in Cs-Te binary systems

Ying Yang,[1,*] Jianhua Wang,[2,*] Ying Liu,[3,†] Yuting Cui,[1] Guangqian Ding,[4] and Xiaotian Wang[2,5,‡]

[1]*College of Physics and Electronic Engineering, Chongqing Normal University, Chongqing 401331 China*

[2]*School of Physical Science and Technology, Southwest University, Chongqing 400715, China*

[3]*School of Materials Science and Engineering, Hebei University of Technology, Tianjin 300130, China*

[4]*School of Science, Chongqing University of Posts and Telecommunications, Chongqing 400065, China*

[5]*Institute for Superconducting and Electronic Materials (ISEM), University of Wollongong, Wollongong 2500, Australia*

(Received 14 November 2022; revised 21 December 2022; accepted 10 January 2023; published 18 January 2023)

In this paper, we used symmetry analyses and first-principles calculations to discover seven Cs-Te binary systems that have different crystal structures and can host symmetry-enforced topologically nontrivial phonons: $P2_12_12_1$-Cs_2Te, *Pbam*-CsTe, *Pnma*-Cs_2Te, $Pm\bar{3}m$-CsTe, *Cmcm*-Cs_2Te_5, *Cmc*2_1-Cs_2Te_3, and $P2_1/c$-$CsTe_4$. These phonons include charge-two Dirac point phonons, charge-one Weyl point phonons, quadratic contact triple point phonons, triple point phonons, butterflylike Weyl nodal line phonons, Dirac nodal line phonons, Weyl nodal loop phonons, multiple straight Weyl nodal line phonons, nodal cage phonons, one-nodal surface phonons, two-nodal surface phonons, and three-nodal surface phonons. Furthermore, the relationship between the crystal structure and the topological properties was thoroughly investigated in this study. More importantly, the Cs-Te binary systems clearly exhibit phononic arc-shaped, phononic nodal-line-shaped, phononic drumheadlike, and phononic torus surface states, which benefit experimental detections. Our theoretical results not only propose various experimentally prepared Cs-Te binary systems with exotic topological phonons and phononic surface states but also explain the structure-property relationship for Cs-Te binary systems based on symmetry analyses.

DOI: 10.1103/PhysRevB.107.024304

I. INTRODUCTION

Over the last decade, various topological quasiparticles in 3D crystalline solids [1], such as nodal points [2–10], nodal lines [11–20], and nodal surfaces [21–25], have received widespread attention because of their unique physical properties and potential applications. Topological quasiparticles have been discovered to exist in spinless systems, such as phonons and various artificial periodic systems (e.g., acoustic/photonic crystals, electric circuit arrays, and mechanical networks) [25–30]. Recently, the study of topological quasiparticles in phonons [31–36], which describe the atomic lattice vibrations in solids, has received significant interest.

Several researchers have used first-principles calculations and symmetry analyses to propose nodal point phonons with different numbers of degeneracies (e.g., twofold degenerate Weyl point phonons [37–44], threefold triple point (TP) phonons [45,46], fourfold degenerate Dirac point phonons [47,48], and sixfold degenerate nodal point phonons) [49–51], different topological charges [37,39], and different orders of dispersion around a band degeneracy [37,39] (such as quadratic contact TP (QCTP) phonons, quadratic Dirac point phonons, quadratic Dirac point, and quadratic TP phonons). Interestingly, Miao *et al.* [38] verified the presence of double-Weyl point phonons in FeSi using inelastic x-ray scattering. Nodal line phonons with different degeneracy types [52], dispersion types [53,54], quadratic orders of dispersion [53], and geometric shapes (such as nodal chain phonons [55–58], nodal box phonons [56], nodal net phonons [59,60], nodal link phonons [60,61], nodal cage phonons [62], and straight nodal line phonons [63]) have been proposed in theory. Remarkably, Zhang *et al.* [64] demonstrated that helical nodal lines exist in the phonon dispersion of MoB_2 by combining first-principles calculation and meV-resolution inelastic x-ray scattering. Furthermore, Liu *et al* [65] and Xie *et al.* [66,67] proposed one-nodal surface phonons, two-nodal surface phonons, and three-nodal surface phonons. It is worth noting that three-nodal surface phonons can be used to achieve the beyond no-go-theorem Weyl phonons [67].

In this paper, we focused on the topological phonons and related phononic surface states in realistic Cs-Te systems. No theoretical study has systematically investigated the topological phonons in Cs-Te systems. The following are the reasons why we chose Cs-Te phases as targets for studying topological phonons: (1) There are numerous stable and metastable phases for Cs-Te systems [68] that can be studied for their topological phonons. (2) Experiments have advanced greatly in the investigation of the phase diagram of Cs-Te materials [69]. Herein, we present seven Cs-Te binary systems with different crystal structures and space groups ($P2_12_12_1$-Cs_2Te, *Pbam*-CsTe, *Pnma*-Cs_2Te, $Pm\bar{3}m$-CsTe, *Cmcm*-Cs_2Te_5, *Cmc*2_1-Cs_2Te_3, and $P2_1/c$-$CsTe_4$) and discuss their related topological phonons in detail.

The topological phonons in these Cs-Te systems have the following advantages: (i) Almost all of these Cs-Te systems

*These authors contributed equally to this paper.

†Corresponding author: ying_liu@hebut.edu.cn

‡Corresponding author: xiaotianwang@swu.edu.cn

can support the coexistence of topological phonons in different dimensions. It should be noted that it would be interesting to study the entanglement between zero-dimensional, one-dimensional, and 2D topological phonons if they coexisted in a single solid-state material. For example, $P2_12_12_1$-Cs_2Te hosts zero-dimensional nodal point phonons and 2D nodal surface phonons. *Pbam*-CsTe hosts zero-dimensional nodal point phonons, one-dimensional nodal line phonons, and 2D nodal surface phonons. (ii) These Cs-Te systems notably exhibit almost all types of phononic surface states, including phononic arc-shaped, drumheadlike, torus-shaped, and nodal-line-shaped surface states. Hence, Cs-Te systems are ideal platforms for further investigating the physical properties of these phononic surface states. Different types of phononic surface states may attract various phononic device applications. (iii) Our theoretical findings not only propose various Cs-Te systems that can exhibit magically topological phonons but also provide structure-property relationships for Cs-Te binary systems based on symmetry analyses.

II. METHODS

The first-principles calculations have been performed within the framework of density functional theory [70], and the projected augmented wave method is applied as implemented in the VIENNA AB INITIO SIMULATION PACKAGE (VASP) [71]. We employed the generalized gradient approximation with the Perdew-Burke-Ernzerhof formalism for the exchange-correlation function [72] and used the projector-augmented wave method to deal with the core-valence interactions [73]. For $C2/m$-Cs_5Te_3 ($P2_1/c$-$CsTe_4$/$P2_12_12_1$-Cs_2Te/$Cmc2_1$-Cs_2Te_3 /*Pbam*-CsTe/*Pnma*-Cs_2Te / *Cmcm*-Cs_2Te_5/$Pm\bar{3}m$-CsTe), the energy cutoff of 500 eV was set for the plane-wave basis and a k mesh of $5 \times 5 \times 3$ ($4 \times 5 \times 2/6 \times 3 \times 3/5 \times 5 \times 4/5 \times 3 \times 7/3 \times 6 \times 3/5 \times 5 \times 3/7 \times 7 \times 7$) Monkhorst-Pack grid was sampled for the first Brillouin zone. For the structure relaxation and self-consistent iteration, the calculation is fully converged until the total residual force per atom is less than -0.01 eV/Å and the total energy variation per atom is smaller than 1×10^{-6} eV.

We used the density functional perturbation theory to obtain the force constants for phonon spectrum calculations, and then we used the PHONOPY package [74] to calculate the phonon dispersion spectrum. We obtained the phonon Hamiltonian of the tight-binding model and the surface local DOSs with the open-source software WANNIER TOOLS [75] and surface Green's functions [76].

III. STABILITY AND CONVEX HULL

The structural stability of Cs-Te systems can be evaluated from the formation energy defined as follows [68]:

$$E_{\text{form}}(Cs_xTe_{1-x}) = E(Cs_xTe_{1-x}) - [xE(Cs) + (1-x)E(Te)], \quad (1)$$

where $E(Cs_xTe_{1-x})$ is the energy per atom of the binary compound while $E(Cs)$ and $E(Te)$ are its counterparts for the most stable elemental phases. Note that the phase diagram of Cs-Te materials has already been constructed based on experimental data in Ref. [69]. The six synthesized phases reported in the phase diagram of Ref. [69], including $C2/m$-Cs_5Te_3 [SG 12], $P2_1/c$-$CsTe_4$ [SG 14], $Cmc2_1$-Cs_2Te_3 [SG 36], *Pbam*-CsTe [SG 55], *Pnma*-Cs_2Te [SG 62], and *Cmcm*-Cs_2Te_5 [SG 63] are located at the convex hull in our calculations. As shown in Fig. 1, we exhibited the formation energies for eight Cs-Te phases, and these values are obtained from DFT total energies in the VASP code. Furthermore, the corresponding values extracted from the Open Quantum Materials Database (OQMD) [77] are also displayed in Fig. 1 as well. Obviously, the values of the E_{form} calculated in this paper are in good agreement with the values in the OQMD. The $Pm\bar{3}m$-CsTe [SG 221] is a metastable phase; however, the $P2_12_12_1$-Cs_2Te [SG 19] is a stable phase.

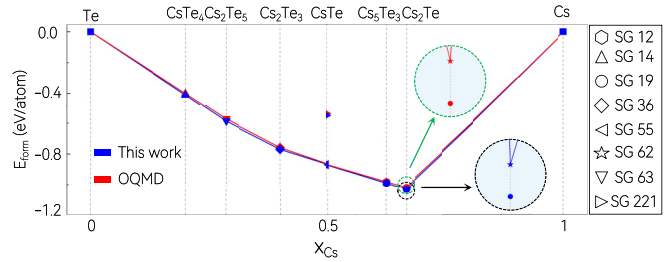

FIG. 1. Formation energies (E_{form}), including the convex hull versus relative Cs concentration.

Moreover, we calculated all the band structures for the eight Cs-Te phases, including $C2/m$-Cs_5Te_3 [SG 12], $P2_1/c$-$CsTe_4$ [SG 14], $P2_12_12_1$-Cs_2Te [SG 19], $Cmc2_1$-Cs_2Te_3 [SG 36], *Pbam*-CsTe [SG 55], *Pnma*-Cs_2Te [SG 62], *Cmcm*-Cs_2Te_5 [SG 63], and $Pm\bar{3}m$-CsTe [SG 221]. All eight Cs-Te phases are semiconductors. The band structures and the related band gaps are shown in Figs. S1 and S2 (see Supplemental Material (SM) [78]).

In the following sections, we come to investigate the topological signatures in the phonon dispersions for $P2_12_12_1$-Cs_2Te [SG 19], *Pbam*-CsTe [SG 55], *Pnma*-Cs_2Te [SG 62], $Pm\bar{3}m$-CsTe [SG 221], *Cmcm*-Cs_2Te_5 [SG 63], $Cmc2_1$-Cs_2Te_3 [SG 36], and $P2_1/c$-$CsTe_4$ [SG 14] one by one. Note that the phonon dispersion for $C2/m$-Cs_5Te_3 [SG 12] is shown in Fig. S3 in the SM [78], and no obvious topological signatures can be found.

IV. CHARGE-TWO DIRAC POINT PHONONS, CHARGE-ONE WEYL POINT PHONONS, THREE-NODAL SURFACE PHONONS, AND PHONONIC ARC-SHAPED SURFACE STATES IN $P2_12_12_1$-Cs_2Te

Figure 2(a) depicts the crystal structure of $P2_12_12_1$-Cs_2Te. One unit cell contains eight Cs atoms and four Te atoms, with optimized lattice constants of a = 5.883 Å, b = 9.608 Å, and c = 11.643 Å, which are similar to the experimental lattice constants of a = 5.867 Å, b = 9.109 Å, and c = 11.486 Å reported by Maeda *et al.* [79] in 2009. Figure 2(c) depicts the phonon dispersion of α-Cs_2Te along high-symmetry paths [see Fig. 2(b)].

Figure 2(c) shows that all the phonon bands along the *X*-*S*-*R*-*U*-*X*, *S*-*R*-*T*-*Y*-*S*, and *U*-*Z*-*T*-*R*-*U* paths (see the gray background) are doubly degenerate, forming three-nodal surface phonons on the $k_i = \pi$ ($i = x, y,$ and z) planes. The three-nodal surface phonons in α-Cs_2Te with space group

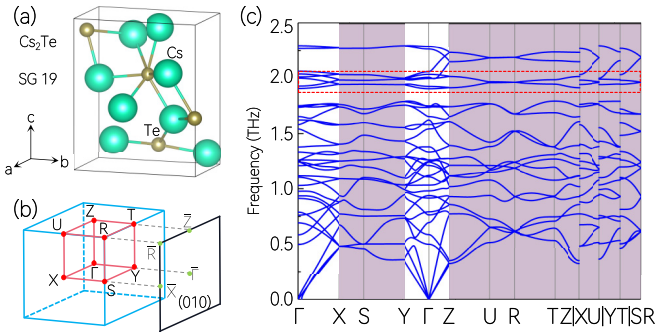

FIG. 2. (a) Crystal structure of $P2_12_12_1$-Cs_2Te; (b) 3D bulk and 2D surface Brillouin zones (BZs). (c) Phonon dispersion of α-Cs_2Te along the Γ-X-S-Y-Γ-Z-U-R-T-$Z|X$-$U|Y$-$T|S$-R high-symmetry paths. The phonon bands with a gray background in (c) can form nodal surface phonons.

$P2_12_12_1$ are symmetry dominated, and such a nodal surface is protected by the combination of a time-reversal symmetry ($\mathcal{T}$) and twofold screw rotation symmetry (S_{2i}).

Consider S_{2i} along the z axis as a typical example without losing generality. This is equivalent to S_{2z}: $(x, y, z) \rightarrow (-x, -y, z + \frac{1}{2})$ with a half translation in the lattice constant along its rotation axis. It also affects the momentum space: S_{2z}: $(k_x, k_y, k_z) \rightarrow (-k_x, -k_y, k_z)$, thereby only preserving the momentum along k_z. The spin-orbit coupling (SOC) for phonon systems is not considered, and $S_{2z}^2 = \mathcal{T}_{100} = e^{-ik_z}$ (where $\mathcal{T}_{100}$ is the translation along the z direction). Moreover, $\mathcal{T}^2 = 1$, which is antiunitary and inverses the momentum $\mathbf{k}$. Consequently, $\mathcal{T}S_{2z}$ is also antiunitary. Additionally, $(\mathcal{T}S_{2z})^2 = e^{-ik_z}|_{k_z=\pm\pi} = -1$ on the $k_z = \pm\pi$ planes, reflecting the appearance of a Kramer-like degeneracy on these planes. Therefore, all the phonon bands on the $k_i = \pm\pi$ ($i = x$, y, and z) planes must become twofold degenerate, resulting in three-nodal surface phonons in α-Cs_2Te with space group $P2_12_12_1$.

Thereafter, we focused on the frequency region around 2.0 THz, and the enlarged figure of the phonon bands in this region is exhibited in Fig. 3(a). Note that $P2_12_12_1$-Cs_2Te with chiral space group 19 can host both charge-two Dirac point phonons and charge-one Weyl point phonons. As shown in Fig. 3(a), the crossing of Nos. 29-32 phonon bands formed a fourfold degenerate Dirac point at the R high-symmetry point, whereas the crossing of Nos. 30 and 31 phonon bands formed twofold degenerate Weyl points on X'-Γ-X paths. The 3D plots of the phonon bands around the Dirac point and the pair of Weyl points are also exhibited in Figs. 3(b) and 3(c). Note that there are no other phonon band crossings around 1.96 THz besides the Weyl and Dirac points, indicating that the topological nodal point phonons in $P2_12_12_1$-Cs_2Te are very clean and ideal. Hence, $P2_12_12_1$-Cs_2Te can be viewed as an ideal platform for realizing the coexistence of Dirac and Weyl phonons. More importantly, the Dirac and Weyl points are topologically nontrivial because they host nonzero Chern numbers. The evolution of the sum of WCCs for the Weyl point and Dirac point are shown in Figs. 3(d) and 3(e), respectively, to determine the topological charges for the points. Notably, the Dirac point at R and the Weyl point on Γ-X have

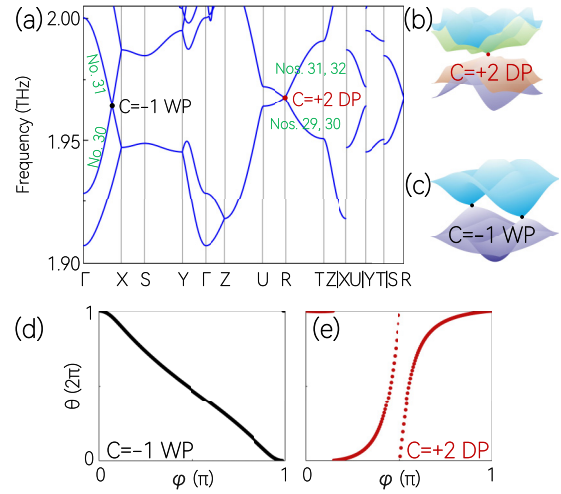

FIG. 3. (a) Enlarged phonon dispersions around 1.95 THz. The 3D plots of (b) the Dirac point with a topological charge of +2 and (c) the pair of Weyl points with a topological charge of −1. The evolution of the sum of the Wannier charge centers (WCCs) on the sphere that encloses the (d) Weyl point and (e) Dirac point, respectively.

topological charges of 2 and −1, respectively. Figure 3(c) shows that there is an equivalent Weyl point with a topological charge of −1 on the X'-Γ path; thus, one charge-two Dirac point (topological charge = +2 and two charge-one Weyl points (topological charge = −1) coexist in $P2_12_12_1$-Cs_2Te. The Nielsen-Ninomiya no-go theorem is satisfied [80,81] because $P2_12_12_1$-Cs_2Te has zero net topological charges.

Figure 4(a) depicts the phonon local density of states (LDOSs) projected on the $P2_12_12_1$-Cs_2Te (010) surface. There are visible phononic arc-shaped surface states that connect the Dirac point and Weyl point projections. Figures 4(b) and 4(c) show the isofrequency surface contours of the (010) surface at various frequencies (1.966 THz, 1.969 THz, 1.967 THz, and 1.965 THz). The phonon surface arcs terminated at $\bar{R}$ [the red balls located at the corner in Figs. 4(b) and 4(c)] are shared by another charge-one Weyl point in the

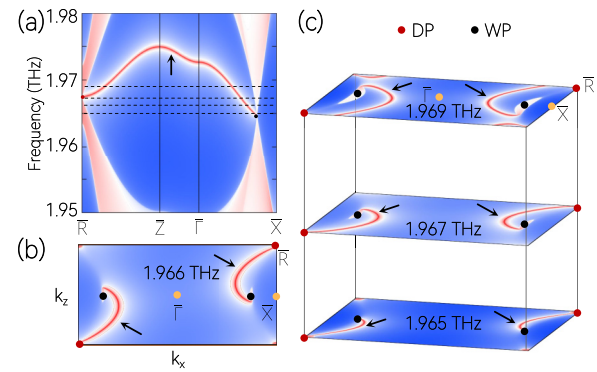

FIG. 4. (a) Phonon local density of states projected on the (010) surface of $P2_12_12_1$-Cs_2Te. (b), (c) Isofrequency surface contours of the (010) surface at different frequencies (1.966 THz, 1.969 THz, 1.967 THz, and 1.965 THz). The phononic arc-shaped surface states are indicated by arrows.

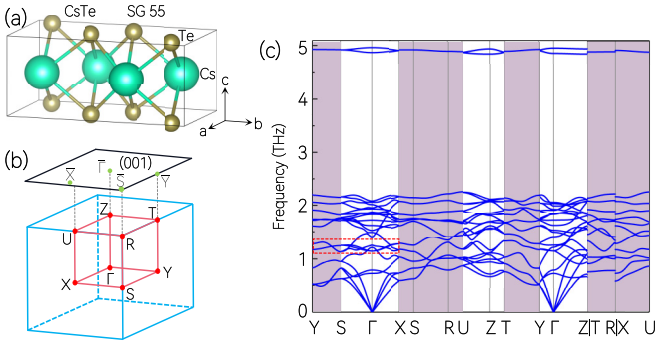

FIG. 5. (a) Crystal structure of *Pbam*-CsTe and (b) 3D bulk and 2D surface BZs. (c) Phonon dispersion of α-CsTe along the Y-S-Γ-X-S-R-U-Z-T-Y-Γ-$Z|T$-$R|X$-U high-symmetry paths. The phonon bands with a gray background in (c) can form nodal surface phonons.

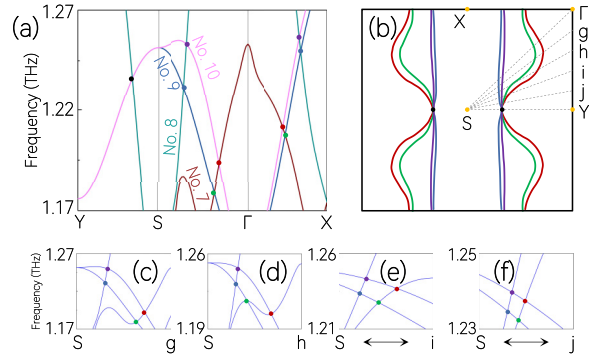

FIG. 6. (a) Enlarged phonon dispersion along the Y-S-Γ-X paths around 1.22 THz. (b) Schematic of four butterflylike Weyl nodal lines (highlighted by different colors) on the $k_z = 0$ plane. The four butterflylike Weyl nodal lines were formed by the crossings of No. 8 and No. 9 phonon bands, No. 8 and No. 10 phonon bands, No. 7 and No. 9 phonon bands, and No. 7 and No. 10 phonon bands, respectively. The jointed point on S-Y for these four Weyl nodal lines is a Dirac point. (c)–(f) Enlarged phonon dispersions along the selected k-paths. Four crossing points with different colors are visible on these selected k paths.

neighboring BZ, which is constrained by topological chiral charges.

V. TWO-NODAL SURFACE PHONONS, DIRAC POINT PHONONS, BUTTERFLY-LIKE WEYL NODAL LINE PHONONS, AND PHONONIC NODAL-LINE-SHAPED SURFACE STATES IN *Pbam*-CsTe

We investigated the topological phonons and related phononic surface states in *Pbam*-CsTe. Figure 5(a) depicts the crystal structure of α-CsTe. Note that the lattice constants obtained from the first-principles calculation were a = 6.322 Å, b = 11.819 Å, and c = 5.103 Å, which agree well with previous experimental results [82] (a = 6.131 Å, b = 11.164 Å, and c = 4.976 Å). Figure 5(c) depicts the phonon dispersion of the α-CsTe primitive cell along the Y-S-Γ-X-S-R-U-Z-T-Y-Γ-$Z|T$-$R|X$-U paths [see Fig. 5(b)]. A supercell of $2 \times 2 \times 2$ is adopted for the calculation of force constants. The phonon bands along the Y-S-R-T-Y and X-S-R-U-X paths are twofold degenerate and highlighted with a gray background. Note that the phonon bands along the symmetry paths of the $k_i = \pm\pi$ ($i = x$ and y) planes are doubly degenerate because the Y-S-R-T-Y and X-S-R-U-X paths belong to the $k_{x/y} = \pi$ plane. In other words, two-nodal surface phonons appear on the $k_x = \pm\pi$ and $k_y = \pm\pi$ planes because of the presence of two twofold rotation symmetries (S_{2x} and S_{2y}) in the *Pbam* space group.

Here, we discuss the topological signature of the phonon bands around 1.22 THz [see the red dotted box in Fig. 5(c)]. The enlarged phonon dispersion of the bands in this box is exhibited in Fig. 6(a). Notably, the phonon bands along the S-Γ and X-Γ paths host four doubly degenerate band-crossing points [see Fig. 6(a)]. Note that the doubly degenerate band-crossing points along Γ-S and Γ-X are not isolated and they belong to multiple Weyl nodal lines on the $k_z = 0$ plane [see Fig. 6(b)]. Moreover, we selected a series of symmetry points between Γ and Y points, namely, g, h, i, and j, which are equally spaced between Y and Γ. Figures 6(c)–6(f) depict the calculated phonon dispersions along the S-g, S-h, S-i, and S-j paths, which manifest four crossing points (highlighted with different colors). These four open Weyl nodal lines have a butterflylike shape, and their jointed point is a fourfold degenerate Dirac point that is located on the Y-S path [see Fig. 6(a)].

Figure 7(a) depicts the calculated phonon LDOSs projected on the *Pbam*-CsTe (001) surface along the $\overline{Y}$-$\overline{S}$-$\overline{\Gamma}$-$\overline{X}$-$\overline{S}$ surface paths. Interestingly, there are doubly degenerate surface-line states along the $\overline{Y}$-$\overline{S}$ and $\overline{X}$-$\overline{S}$ surface paths. Figures 7(b)–7(g) show a series of isofrequency surface arcs for different phonon frequencies [see the dotted lines in Fig. 7(a)] to better describe the degenerate surface-line mode along the above-mentioned surface paths. Figures 7(b)–7(g) clearly exhibit surface twofold degenerate points formed by the crossing of two nondegenerate surface modes.

Note that the degenerate surface-line phonon mode in *Pbam*-CsTe (with space group No. 55) along the $\overline{Y}$-$\overline{S}$ and $\overline{X}$-$\overline{S}$ is symmetry dominated. This system hosts two independent glide mirrors: $\widetilde{M}_x : (-x + \frac{1}{2}, y + \frac{1}{2}, z)$ and $\widetilde{M}_y : (x + \frac{1}{2}, -y + \frac{1}{2}, z)$. The surface state along the $\bar{X} - \bar{S}$ ($k_x = \pi$ axis) is invariant under $\mathcal{T}\widetilde{M}_y$. Remarkably, $(\mathcal{T}\widetilde{M}_y)^2 = e^{-ik_x} = -1$ on this surface, resulting in a Kramer-like degeneracy. Furthermore, $(\mathcal{T}\widetilde{M}_x)^2 = e^{-ik_y} = -1$ on the $\bar{Y} - \bar{S}$ ($k_y = \pi$ axis),

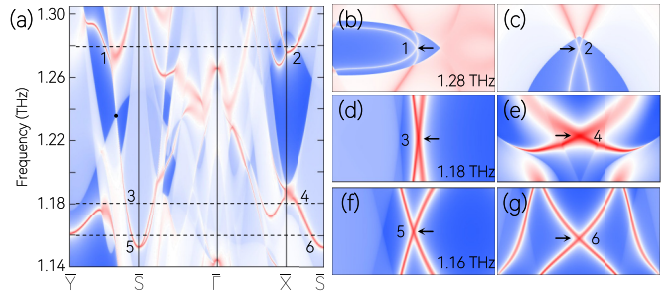

FIG. 7. (a) Phonon LDOSs projected on the *Pbam*-CsTe (001) surface along the $\overline{Y}$-$\overline{S}$-$\overline{\Gamma}$-$\overline{X}$-$\overline{S}$ surface paths. Isofrequency surface arcs for (b), (c) 1.28 THz; (d), (e) 1.18 THz; and (f), (g) 1.16 THz. The surface twofold degenerate crossing points in (b)–(g) are indicated by arrows.

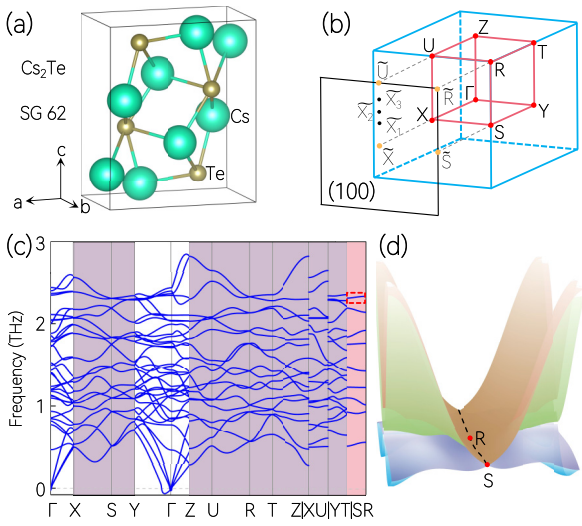

FIG. 8. (a) Crystal structure of *Pnma*-Cs_2Te. (b) 3D bulk and 2D surface BZs. (c) Phonon dispersion of *Pnma*-Cs_2Te along the Γ-*X*-*S*-*Y*-Γ-*Z*-*U*-*R*-*T*-*Z*|*X*-*U*|*Y*-*T*|*S*-*R* high-symmetry paths. (d) 3D plot of the fourfold degenerate Dirac nodal line phonons along the *S*-*R* path. The phonon bands with a gray background in (c) can form nodal surface phonons.

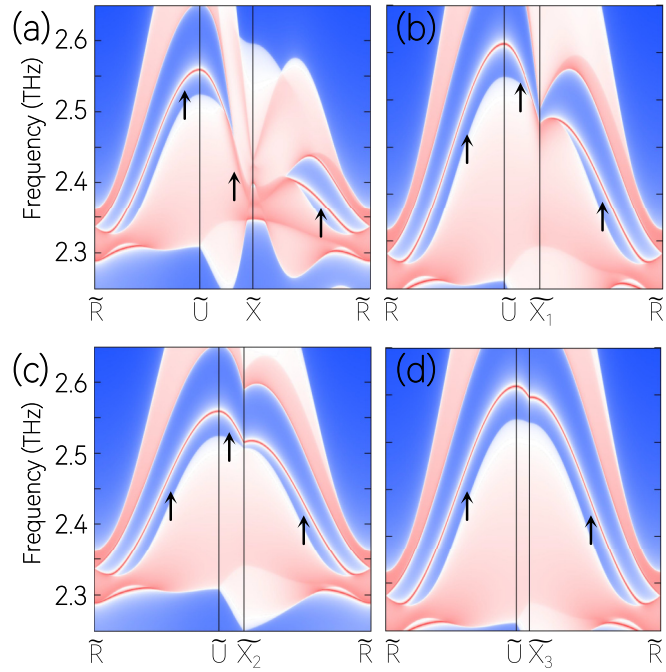

FIG. 9. (a)–(d) Phonon LDOSs projected on the (100) surface for *Pnma*-Cs_2Te along the $\widetilde{R}$-$\widetilde{U}$-$\widetilde{X}$-$\widetilde{R}$, $\widetilde{R}$-$\widetilde{U}$-$\widetilde{X}_1$-$\widetilde{R}$, $\widetilde{R}$-$\widetilde{U}$-$\widetilde{X}_2$-$\widetilde{R}$ and $\widetilde{R}$-$\widetilde{U}$-$\widetilde{X}_3$-$\widetilde{R}$ surface paths, respectively. The phononic torus surface states are highlighted by arrows.

demonstrating that each state on this path is at least double degenerate because of the Kramer-like degeneracy. Thus, states on the $\bar{Y}-\bar{S}$ and $\bar{X}-\bar{S}$ paths are doubly degenerate.

VI. THREE-NODAL SURFACE PHONONS, DIRAC NODAL LINE PHONONS, AND PHONONIC TORUS SURFACE STATES IN *Pnma*-Cs_2Te

Pnma-Cs_2Te can be prepared via the solid-gas reaction described by Prins and Cordfunke [83], and its experimental lattice constants are a = 9.110 Å, b = 5.871 Å, and c = 11.494 Å. The calculated lattice constants for *Pnma*-Cs_2Te were a = 9.599 Å, b = 5.901 Å, and c = 11.612 Å, which are close to the experimental values. Figure 8(a) depicts the crystal structure of *Pnma*-Cs_2Te, in which Cs and Te are located at 4c Wyckoff positions. The symmetry operators for *Pnma*-Cs_2Te are summarized as follows: Two screw rotations, namely, $\widetilde{C}_{2z}=\{C_{2z}|\frac{1}{2}0\frac{1}{2}\}$ and $\widetilde{C}_{2y}=\{C_{2y}|0\frac{1}{2}0\}$, a spatial inversion $\mathcal{P}$, and $\mathcal{T}$ with $\mathcal{T}^2=1$ (because it is a spinless system). Figure 8(c) depicts the calculated phonon dispersion of the *Pnma*-Cs_2Te primitive cell along the Γ-*X*-*S*-*Y*-Γ-*Z*-*U*-*R*-*T*-*Z*|*X*-*U*|*Y*-*T*|*S*-*R* paths. A supercell of $2\times2\times2$ is adopted for the calculation of force constants. Figure 8(c) shows that the phonon bands along the *X*-*U*-*R*-*S*-*X*, *S*-*R*-*T*-*Y*-*S* and *U*-*R*-*T*-*Z*-*U* paths are at least twofold degenerate; therefore, there are three-nodal surface phonons on the $k_i=\pm\pi$ ($i=x,y,$ and z) planes. The following can be deduced as the cause based on the symmetry analyses: *Pnma*-Cs_2Te hosts three orthogonal twofold screw rotation axes. By considering a combined antiunitary operation $\mathcal{T}\widetilde{C}_{2i}$ ($i=x,y,z$), it can be easily derived that $(\mathcal{T}\widetilde{C}_{2i})^2=e^{ik_i}$. Consequently, $(\mathcal{T}\widetilde{C}_{2i})^2=-1$ at the corresponding plane, $k_i=\pi$. That is, the phonon bands along all boundary planes ($k_{x/y/z}=\pi$) are at least twofold degenerate.

Interestingly, the phonon bands along the *S*-*R* path are fourfold degenerate, reflecting the presence of multiple Dirac nodal line phonons [see the box with red background in Fig. 8(c)]. Figure 8(d) displays the 3D plot of the shape of one Dirac nodal line phonons around 2.5 THz along the *S*-*R* path as an example. The appearance of the Dirac nodal line phonons can be determined from the aspect of symmetry. Figure 8(d) shows that the Dirac nodal line lies at the hinge between the $k_x=\pi$ and $k_y=\pi$ planes; it comprises invariant subspaces of $\widetilde{C}_{2z}$ and $\widetilde{M}_y$ and a combined operation $\mathcal{T}\widetilde{C}_{2x}$, where $\widetilde{C}_{2x}=\mathcal{P}\widetilde{C}_{2z}\widetilde{M}_y$. The commutations between them are expressed as $\widetilde{C}_{2z}\widetilde{M}_y=\mathcal{T}_{010}\widetilde{M}_y\widetilde{C}_{2z}$ and $\widetilde{M}_y(\mathcal{T}\widetilde{C}_{2x})=(\mathcal{T}\widetilde{C}_{2x})\widetilde{M}_y$, where $\mathcal{T}_{010}$ is the translation along the y direction.

Furthermore, $\{\widetilde{C}_{2z},\widetilde{M}_y\}=0$ and $[\widetilde{M}_y,(\mathcal{T}\widetilde{C}_{2x})]=0$ along the *S*-*R* path. The Bloch states along this path can be chosen as the eigenstates of $\widetilde{M}_y$. Without SOC, $\widetilde{M}_y{}^2=1$, such that $g_y=\pm1$. The Bloch states can be characterized by $\widetilde{M}_y$ eigenvalues denoted as $|g_y=\pm1\rangle$. If $|g_y=1\rangle$ is used as a typical example, then $(\mathcal{T}\widetilde{C}_{2x})^2=-1$ along this path, which indicates a Kramer-like degeneracy. Thus, $|g_y=1\rangle$ and $\mathcal{T}\widetilde{C}_{2x}|g_y=1\rangle$ are degenerate and share the same eigenvalues. Additionally, since $\widetilde{C}_{2z}\widetilde{M}_y=\mathcal{T}_{010}\widetilde{M}_y\widetilde{C}_{2z}$, the anticommutation relationship also implies that $|g_y=1\rangle$ and $\widetilde{C}_{2z}|g_y\rangle$ are degenerate, which correspond to the opposite g_y. Consequently, $\{|g_y=1\rangle,\widetilde{C}_{2z}|g_y=1\rangle,\mathcal{T}\widetilde{C}_{2x}|g_y=1\rangle,$ and $\mathcal{T}\widetilde{C}_{2x}\widetilde{C}_{2y}|g_y=1\rangle\}$ are degenerate along this path, indicating that there is indeed a fourfold degenerate Dirac nodal line along the *S*-*R* path.

Figures 9(a)–9(d) depict the calculated (100) surface states for *Pnma*-Cs_2Te along the $\widetilde{R}$-$\widetilde{U}$-$\widetilde{X}$-$\widetilde{R}$, $\widetilde{R}$-$\widetilde{U}$-$\widetilde{X}_1$-$\widetilde{R}$, $\widetilde{R}$-$\widetilde{U}$-$\widetilde{X}_2$-$\widetilde{R}$ and $\widetilde{R}$-$\widetilde{U}$-$\widetilde{X}_3$-$\widetilde{R}$ surface paths, respectively. Figure 9

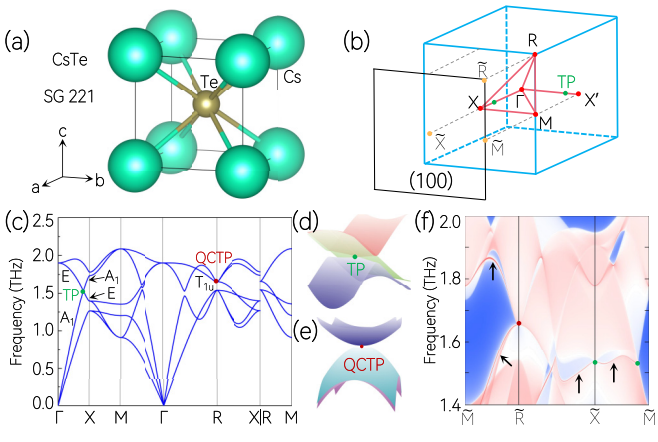

FIG. 10. (a) Crystal structure of $Pm\bar{3}m$-CsTe. (b) 3D bulk and 2D surface BZs. (c) Phonon dispersion of $Pm\bar{3}m$-CsTe along the Γ-X-M-Γ-R-$X|R$-M high-symmetry paths. (d), (e) 3D plots of the threefold degenerate TP and QCTP phonons. (f) Phonon LDOSs projected on the (100) surface for $Pm\bar{3}m$-CsTe. Phononic surface states resulting from the projections of the TPs and QCTPs are indicated by arrows.

shows that phononic surface states (marked by arrows) appear along all the above-mentioned surface paths. In other words, the phononic surface states will span over the entire (100) surface BZ. Such phononic surface states can be referred to as phononic torus surface states because the 2D BZ is a torus. Note that the phononic surface states around $\widetilde{X}$ and $\widetilde{X}_1$ surface points in Figs. 9(a) and 9(b) are somewhat covered by the bulk states. However, the phononic surface states and bulk states in Figs. 9(c) and 9(d) are well separated along the $\widetilde{R}$-$\widetilde{U}$-$\widetilde{X}_2$-$\widetilde{R}$ and $\widetilde{R}$-$\widetilde{U}$-$\widetilde{X}_3$-$\widetilde{R}$ surface paths.

VII. TP AND QCTP PHONONS IN $Pm\bar{3}m$-CsTe

Figure 10(a) exhibits the crystal structure of $Pm\bar{3}m$-CsTe [82]. Figure 10(c) shows the phonon dispersion of the β-CsTe primitive cell along the Γ-X-M-Γ-R-$X|R$-M paths [see Fig. 10(b)]. A supercell of $3\times3\times3$ is adopted for the calculation of force constants. There is a TP on Γ-X and a QCTP at the R high-symmetry point. The QCTP is a zero-dimensional threefold band degeneracy with a topological charge of 0, and it features a quadratic energy splitting along any direction in momentum space [see Fig. 10(e)]. The TP is a zero-dimensional threefold degenerate point formed by the crossing of one nondegenerate band and one twofold degenerate band along the Γ-X [see Fig. 10(d)].

The QCTP at the R point is an essential degeneracy for $Pm\bar{3}m$-CsTe with space group No. 221. The point group at the R point is O_h, which is generated by S_{61}, M_x, M_z, and C_{2c}. This point group has 3D irreducible representations, such as T_{1u}. Accordingly, the generating elements and $\mathcal{T}$ can be expressed as follows:

$$S_{61}=\begin{pmatrix}0&0&1\\1&0&0\\0&1&0\end{pmatrix},\ M_x=\begin{pmatrix}1&0&0\\0&-1&0\\0&0&-1\end{pmatrix},\ M_z=\begin{pmatrix}-1&0&0\\0&-1&0\\0&0&1\end{pmatrix},\ C_{2c}=\begin{pmatrix}0&0&1\\0&-1&0\\1&0&0\end{pmatrix},\ \mathcal{T}=\begin{pmatrix}1&0&0\\0&1&0\\0&0&1\end{pmatrix}\mathcal{K}, \tag{2}$$

where $\mathcal{K}$ is the complex conjugation. Constrained by these operations, the effective model around the QCTP can be described using another effective model:

$$\mathcal{H}_{\mathrm{QCTP}}=\begin{pmatrix}Ak_y^2+B(k_x^2+k_z^2)&Ck_xk_y&Ck_zk_y\\Ck_xk_y&Ak_x^2+B(k_y^2+k_z^2)&Ck_xk_z\\Ck_zk_y&Ck_xk_z&Ak_z^2+B(k_x^2+k_y^2)\end{pmatrix}. \tag{3}$$

This effective model clearly demonstrates that the dispersion around this point is quadratic.

Moreover, the TP on the Γ-X path has an accidental degeneracy between a double degeneracy and a single band, namely, $\{E, A_1\}$. Based on these two irreducible representations, the independent generating elements on this path, namely, $\{C_{4y}, M_x, \mathcal{PT}\}$, can be expressed as

$$C_{4y}=\begin{pmatrix}1&0&0\\0&0&-1\\0&1&0\end{pmatrix},\ M_x=\begin{pmatrix}-1&0&0\\0&1&0\\0&0&-1\end{pmatrix},\ \mathcal{PT}=\begin{pmatrix}1&0&0\\0&-1&0\\0&0&-1\end{pmatrix}\mathcal{K}. \tag{4}$$

Thus, the effective model that describes the TP on the Γ-X path can be expressed as

$$\mathcal{H}_{TP}=(c_0+c_1k_y)I_{3\times3}+\begin{pmatrix}2c_2k_y&ic_3(k_x-k_z)&0\\-ic_3(k_x-k_z)&-c_2k_y&0\\0&0&-c_2k_y\end{pmatrix}. \tag{5}$$

Contrary to the QCTP, the TP exhibits a linear dispersion in all directions.

Figure 10(f) plots the phonon LDOSs projected on the (100) surface for $Pm\bar{3}m$-CsTe. The TPs located on the Γ-X and Γ-X' paths and the QCTP at the R high-symmetry point are projected onto the (100) surface. The arc-shaped surface states that connect these projected crossing points are visible.

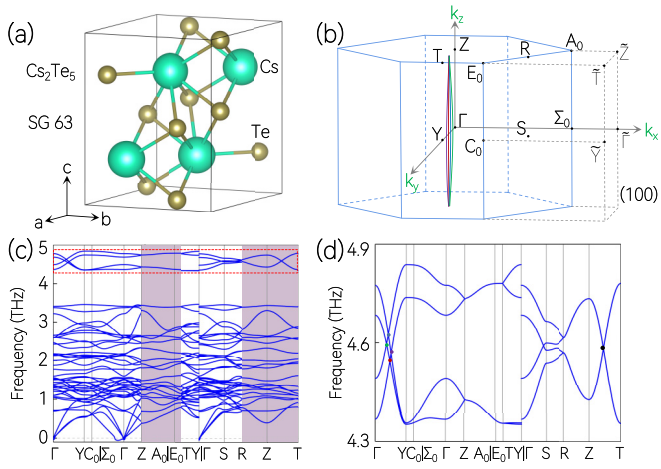

FIG. 11. (a) Crystal structure of *Cmcm*-Cs_2Te_5. (b) 3D bulk and 2D surface BZs. (c) Phonon dispersion of *Cmcm*-Cs_2Te_5 along the Γ-Y-$C_0|\Sigma_0$-Γ-Z-$A_0|E_0$-T-$Y|\Gamma$-S-R-Z-T high-symmetry paths. (d) Enlarged phonon bands in the red dotted box in (c). The phonon bands with a gray background in (c) can form nodal surface phonons.

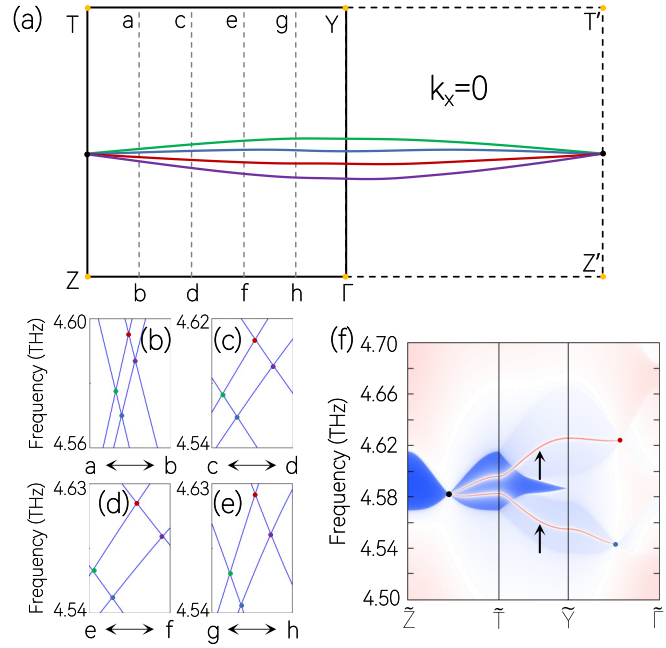

FIG. 12. (a) Schematic of the four Weyl nodal loops (highlighted by different colors) on the $k_x = 0$ plane. In (a), a, c, e, and g (b, d, f, and h) are equally divided between T and Y (Z and Γ). (b)–(e) Enlarged phonon dispersions along the a-b, c-d, e-f, and g-h paths, respectively. (f) Phonon LDOSs projected on the (100) surface of *Cmcm*-Cs_2Te_5. The arrows indicate phononic surface states resulting from the projections of the Dirac point and Weyl points.

VIII. MULTIPLE WEYL NODAL LOOP PHONONS, ONE-NODAL SURFACE PHONONS, AND DIRAC POINT PHONONS IN *Cmcm*-Cs_2Te_5

Next, we investigated the topological signatures for the phonon bands of *Cmcm*-Cs_2Te_5. Microcrystalline Cs_2Te_5 [84] can be obtained from stoichiometric batches of pure elements in supercritical ammonia. The experimental lattice constants for *Cmcm*-Cs_2Te_5 are a = b = 7.723 Å, and c = 10.12 Å, and the lattice constants determined from the first-principles calculations were a = b = 7.748 Å, and c = 10.336 Å. Figure 11(a) depicts the crystal structure of the primitive *Cmcm*-Cs_2Te_5 cell. Figure 11(c) depicts the phonon dispersion of the *Cmcm*-Cs_2Te_5 primitive cell along the Γ-Y-$C_0|\Sigma_0$-Γ-Z-$A_0|E_0$-T-$Y|\Gamma$-S-R-Z-T paths. A supercell of $2 \times 2 \times 2$ is adopted for the calculation of force constants. The phonon bands along the Z-$A_0|E_0$-T-Z-R paths with a gray background are twofold degenerate, reflecting the presence of one-nodal surface phonons on the $k_z = \pm\pi$ planes. Thereafter, we focused on the phonon bands around 4.6 THz [see the red dotted box in Fig. 11(c)]. The enlarged phonon dispersion is displayed in Fig. 11(d). Notably, one fourfold degenerate Dirac point and four twofold degenerate Weyl points can be found on the Z-T and Γ-Y paths, respectively. As shown in Figs. 12(b)–12(e), the four twofold degenerate Weyl points can also be found on the a-b, c-d, e-f, and g-h symmetry paths, confirming the presence of four Weyl nodal lines on the $k_x = 0$ plane. Figure 12(a) depicts the schematic of the four Γ-centered Weyl nodal loops, in which two fourfold Dirac points appear as the jointed points of the multiple Weyl lines on the Z-T and Z'-T' paths. Phonon LDOSs projected on the (100) surface [see Fig. 11(b)] are shown in Fig. 12(f). Note that the multiple Weyl nodal line phonons in *Cmcm*-Cs_2Te_5 are closed and are considerably different from the multiple open Weyl nodal line phonons in *Pbam*-CsTe [see Fig. 6(b)].

IX. ONE-NODAL SURFACE PHONONS, WEYL NODAL LOOP PHONONS, AND PHONONIC DRUMHEAD-LIKE SURFACE STATES IN *Cmc*2_1-Cs_2Te_3

We would like to emphasize that Weyl nodal loop phonons can also be found in *Cmc*2_1-Cs_2Te_3, which is a realistic material prepared by Böttcher in 1980 [85]. The experimental lattice constants are a = b = 7.427 Å, and c = 8.68 Å, and the lattice constants obtained from the first-principles calculation were a = b = 7.607 Å, and c = 8.752 Å. We calculated the phonon dispersion of the *Cmc*2_1-Cs_2Te_3 primitive cell along the Γ-Y-$C_0|\Sigma_0$-Γ-Z-$A_0|E_0$-T-$Y|\Gamma$-S-R-Z-T paths [see Fig. 13(b)] based on the relaxed crystal structures in Fig. 13(a). A supercell of $2 \times 2 \times 2$ is adopted for the calculation of force constants. Figure 13(c) displays the results, which reveal that one-nodal surface phonons can be found on the $k_z = \pm\pi$ planes.

More interestingly, a series of phonon crossing points can be found around 4.4 THz. Specifically, two doubly degenerate points are located on Γ-Σ_0, and one doubly degenerate point is located on the Γ-Z path [see Fig. 13(d)]. These three crossing points are all located on the $k_y = 0$ plane. Figures 14(a) and 14(b) show that the doubly degenerate crossing points occur on the Γ-$a/b/c/d/e/f/g/h$ paths. Therefore, these doubly degenerate points are not isolated, and they belong to multiple Weyl nodal loops on the $k_y = 0$ plane.

Figure 14(c) shows the phonon LDOSs projected on the (010) surface of *Cmc*2_1-Cs_2Te_3. As shown in Fig. 13(b), some crossing points of the Weyl loops are projected onto the (010) surface. Figure 14(c) shows phononic drumheadlike surface

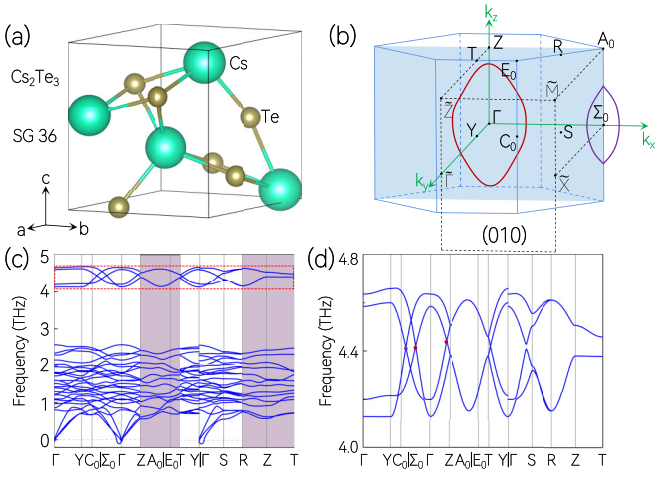

FIG. 13. (a) Crystal structure of $Cmc2_1$-Cs_2Te_3. (b) 3D bulk and 2D surface BZs. (c) Phonon dispersion of $Cmc2_1$-Cs_2Te_3 along the Γ-Y-$C_0|\Sigma_0$-Γ-Z-$A_0|E_0$-T-$Y|\Gamma$-S-R-Z-T high-symmetry paths. (d) Enlarged phonon bands in the red dotted box in (c). The phonon bands with a gray background in (c) can form nodal surface phonons.

states arising from the projections of the crossing points of the closed Weyl nodal loops. We would like to emphasize that the visible drumheadlike surface states will benefit experimental detections.

X. ONE-NODAL SURFACE PHONONS, MULTIPLE STRAIGHT WEYL NODAL LINE PHONONS, AND NODAL CAGE PHONONS IN $P2_1/c$-$CsTe_4$

Figure 15(a) shows the crystal structure of $P2_1/c$-$CsTe_4$, which is monoclinic and can be obtained from a melting reaction at 570 °C in sealed quartz tubes [86]. The experimental lattice constants for $P2_1/c$-$CsTe_4$ are a = 7.857 Å, b = 7.286 Å, and c = 14.155 Å. Our theoretical lattice constants were a = 8.158 Å, b = 7.359 Å, and c = 14.271 Å. Figure 15(d) depicts the calculated phonon dispersion of $P2_1/c$-$CsTe_4$ along the Γ-Z-D-B-Γ-A-E-Z-C-Y-Γ paths [see Fig. 15(b)].

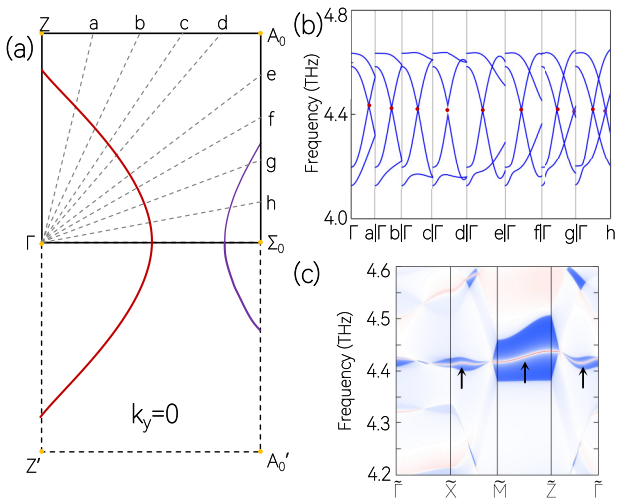

FIG. 14. (a) Schematic of the Weyl nodal loops (highlighted by different colors) on the $k_y = 0$ plane. In (a), a, b, c, and d (e, f, g, and h) are equally divided between Z and A_0 (A_0 and Σ_0). (b) Enlarged phonon dispersions along the Γ-$a/b/c/d/e/f/g/h$ paths, respectively. (c) Phonon LDOSs projected on the (010) surface of $Cmc2_1$-Cs_2Te_3. The arrows indicate phononic surface states resulting from the projections of the crossing points of the Weyl loops.

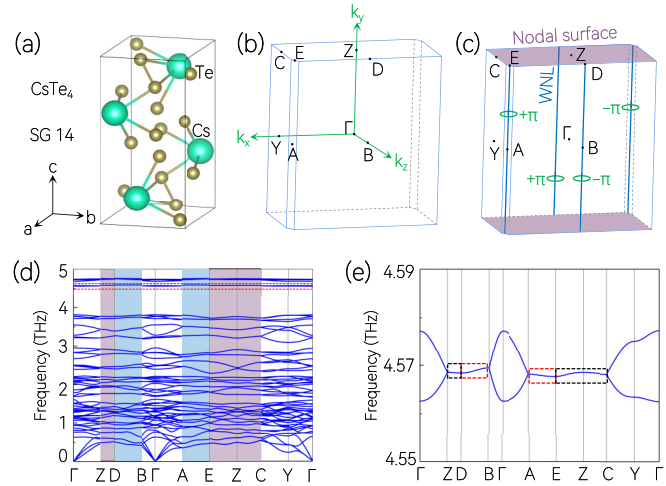

FIG. 15. (a) Crystal structure of $P2_1/c$-$CsTe_4$. (b) 3D bulk BZ. (c) Schematic of nodal cage phonons formed by the one-nodal surface phonons and straight nodal line phonons. (d) Phonon dispersion of $P2_1/c$-$CsTe_4$ along the Γ-Z-D-B-Γ-A-E-Z-C-Y-Γ high-symmetry paths. The phonon bands with a gray background in (d) can form nodal surface phonons. The phonon bands with a blue background can form straight Weyl nodal line phonons. (e) Enlarged figure of the phonon bands marked by the red dotted box in (d).

Figure 15(d) shows that the phonon bands (with a gray background) along the Z-D-E-Z-C paths are doubly degenerate, indicating the appearance of one-nodal surface phonons on the $k_y = \pm\pi$ planes [see Fig. 15(c)]. Meanwhile, the phonon bands [with a blue background in Fig. 15(d)] along the D-B and A-E paths are doubly degenerate, indicating the occurrence of straight Weyl nodal line phonons.

We studied the topological phonons for the phonon bands around 4.57 THz as a typical example. Figure 15(e) depicts the enlarged figure of the phonon bands with the red dotted box in Fig. 15(d). Doubly degenerate phonon bands can be found along the D-B and A-E paths [with red boxes in Fig. 15(e)]. These phonon bands belong to straight Weyl nodal lines [see Fig. 15(c)]. We also calculated the Berry phase for the two closed loops surrounding the straight Weyl nodal lines using the following equation: $P_B = \oint_L A(\mathbf{k})\cdot dk$, where $\boldsymbol{A}(\boldsymbol{k}) = -i\langle\varphi(\boldsymbol{k})|\nabla_{\boldsymbol{k}}|\varphi(\boldsymbol{k})\rangle$ is the Berry connection and $\varphi(\mathbf{k})$ is the periodic part of the Bloch function. Figure 15(c) shows that the P_B values for these straight Weyl nodal lines are equal to $\pm\pi$, indicating that they have topological nontrivial signatures. The phonon bands along the Z-D and E-Z-C paths are doubly degenerate [with black boxes in Fig. 15(e)], and they belong to the one-nodal surface phonons on the $k_y = \pm\pi$ planes. A nodal cage phonon is formed in the 3D BZ [see Fig. 15(c)] when the one-nodal surface phonons on the $k_y = \pm\pi$ planes combine with the straight Weyl nodal line phonons.

XI. SUMMARY AND REMARKS

Herein, seven Cs-Te systems are proposed as candidates that host topological phonons based on first-principles calculation and symmetry analyses: $P2_12_12_1$-Cs_2Te, *Pbam*-CsTe, *Pnma*-Cs_2Te, $Pm\bar{3}m$-CsTe, *Cmcm*-Cs_2Te_5, $Cmc2_1$-Cs_2Te_3, and $P2_1/c$-$CsTe_4$. The main conclusions of this paper are as follows:

(i) $P2_12_12_1$-Cs_2Te can host charge-two Dirac point phonons, charge-one Weyl point phonons, and three-nodal surface phonons. Contrary to the projections of conventional Weyl pairs, which host only one surface arc, the projections of the charge-two Dirac point and the two charge-one Weyl points can be connected to form two surface arcs.

(ii) *Pbam*-CsTe can host two-nodal surface phonons, Dirac point phonons, and butterflylike Weyl nodal line phonons in the 3D BZ. Note that *Pbam*-CsTe is an ideal candidate for investigating the entanglement between the zero-dimensional, one-dimensional, and 2D topological elements in phonons. More importantly, a symmetry-dominated degenerate surface-line phonon mode can be observed in *Pbam*-CsTe (with space group No. 55) along the $\overline{Y}$-$\overline{S}$ and $\overline{X}$-$\overline{S}$ surface paths. To the best of our knowledge, the degeneracy of nodal lines in bulk states has been extensively studied in various quasiparticle band structures, whereas the degeneracy of surface lines has received less attention. Therefore, *Pbam*-CsTe is an excellent candidate for further investigating degenerate surface lines in phonon surface states.

(iii) *Pnma*-Cs_2Te can host three-nodal surface phonons and Dirac nodal line phonons. Moreover, unlike typical phononic drumhead-like surface states, the phononic surface states in Pnma-Cs_2Te span over the entire (100) surface BZ. Such phononic surface states can be referred to as phononic torus surface states because the 2D BZ is a torus.

(iv) $Pm\bar{3}m$-CsTe can host TP and QCTP phonons.

(v) *Cmcm*-Cs_2Te_5 can host one-nodal surface phonons, multiple Weyl nodal loop phonons, and Dirac point phonons. Note that the multiple Weyl nodal line phonons in *Cmcm*-Cs_2Te_5 are closed, which is contrary to the open multiple Weyl nodal line phonons in *Pbam*-CsTe.

(vi) $Cmc2_1$-Cs_2Te_3 can host one-nodal surface phonons and Weyl nodal loop phonons. Moreover, the projections of the crossing points of the Weyl nodal loops result in visible phononic drumheadlike surface states on the (010) surface.

(vii) $P2_1/c$-$CsTe_4$ can host one-nodal surface phonons and multiple straight Weyl nodal line phonons in the 3D BZ. Furthermore, the combination of the one-nodal surface phonons and the multiple straight Weyl nodal line phonons can result in a nodal cage phonon in the 3D BZ.

Before concluding, we would like to emphasize the following two points:

(i) The experimental confirmation of the predicted topological phonons in Cs-Te systems is imminent. The bulk phonon can be imaged by inelastic x-ray scattering [87] or neutron scattering [88] in experiments. The surface phonon modes can be verified by high-resolution electron energy-loss spectroscopy [89], helium atom scattering [90], or THz spectroscopy [91] in experiments.

(ii) Topological phonons may affect observable physical properties or effects of realistic materials. For example, Singh *et al.* [45] proposed that the gapless topological phonon modes in topological phononic materials can provide additional scattering channels in the three phonon-phonon scattering processes to decrease the mean-free path and suppress the lattice thermal conductivity, and possibly enhance the thermoelectric performance. Zhang *et al.* [37] suggested that the surface states of clean topological phonons may enhance the electron-phonon coupling and possibly trigger the topological superconductivity at the surfaces or interfaces. As mentioned in the work of Zhu *et al.* [92], most catalytic processes occur on the surfaces. In some cases, topological surface phonon modes may promote catalysis if the phonon frequency is in resonance with certain midsteps in the reaction. We hope the reported Cs-Te systems with different topological phonons and phononic surface modes can be used as targets to study the related physical properties and possible applications in the near future.

ACKNOWLEDGMENTS

Y.L. is grateful for the support from the Natural Science Foundation of Hebei Province (No. A2021202002). X.W. is grateful for the support from the Natural Science Foundation of Chongqing (No. CSTB2022NSCQ-MSX0283).

[1] Z.-M. Yu, Z. Zhang, G.-B. Liu, W. Wu, X.-P. Li, R.-W. Zhang, S. A. Yang, and Y. Yao, Sci. Bull. **67**, 375 (2022).
[2] T.-T. Zhang, Z.-M. Yu, W. Guo, D. Shi, G. Zhang, and Y. Yao, J. Phys. Chem. Lett. **8**, 5792 (2017).
[3] X. Zhang, Z.-M. Yu, X.-L. Sheng, H. Y. Yang, and S. A. Yang, Phys. Rev. B **95**, 235116 (2017).
[4] Z. Zhu, Y. Liu, Z.-M. Yu, S.-S. Wang, Y. X. Zhao, Y. Feng, X.-L. Sheng, and S. A. Yang, Phys. Rev. B **98**, 125104 (2018).
[5] F. Zhou, C. X. Cui, J. H. Wang, M. Q. Kuang, T. Yang, Z.-M. Yu, X. T. Wang, G. Zhang, and Z. X. Cheng, Phys. Rev. B **103**, 245126 (2021).
[6] Z.-M. Yu, W. Wu, Y. X. Zhao, and S. A. Yang, Phys. Rev. B **100**, 041118(R) (2019).
[7] N. P. Armitage, E. J. Mele, and A. Vishwanath, Rev. Mod. Phys. **90**, 015001 (2018).
[8] S. M. Young and C. L. Kane, Phys. Rev. Lett. **115**, 126803 (2015).
[9] B. J. Yang and N. Nagaosa, Nat. Commun. **5**, 4898 (2014).
[10] B. Yan and C. Felser, Annu. Rev. Condens. Matter Phys. **8**, 337 (2017).
[11] C. Fang, H. Weng, X. Dai, and Z. Fang, Chin. Phys. B **25**, 117106 (2016).
[12] C. Fang, Y. Chen, H.-Y. Kee, and L. Fu, Phys. Rev. B **92**, 081201(R) (2015).
[13] D. S. Ma, J. Zhou, B. Fu, Z. M. Yu, C. C. Liu, and Y. Yao, Phys. Rev. B **98**, 201104(R) (2018).

[14] X.-P. Li, B. Fu, D.-S. Ma, C. Cui, Z.-M. Yu, and Y. Yao, Phys. Rev. B **103**, L161109 (2021).

[15] Z. Zhang, Z. M. Yu, and S. A. Yang, Phys. Rev. B **103**, 115112 (2021).

[16] X. Sheng, Z. Yu, R. Yu, H. Weng, and A. S. Yang, J. Phys. Chem. Lett. **8**, 3506 (2017).

[17] S. Li, Y. Liu, S.-S. Wang, Z.-M. Yu, S. Guan, X.-L. Sheng, Y. Yao, and S. A. Yang, Phys. Rev. B **97**, 045131 (2018).

[18] X. M. Zhang, Z.-M. Yu, Z. M. Zhu, W. K. Wu, S.-S. Wang, X.-L. Sheng, and S. A. Yang, Phys. Rev. B **97**, 235150 (2018).

[19] Z.-M. Yu, W. K. Wu, X.-L. Sheng, Y. X. Zhao, and S. Y. A. Yang, Phys. Rev. B **99**, 121106(R) (2019).

[20] L. Jin, X. M. Zhang, X. F. Dai, L. Y. Wang, H. Y. Liu, and G. D. Liu, IUCrJ **6**, 688 (2019).

[21] W. Wu, Y. Liu, S. Li, C. Zhong, Z.-M. Yu, X.-L. Sheng, Y. X. Zhao, and S. A. Yang, Phys. Rev. B **97**, 115125 (2018).

[22] S. Z. Chen, S. Li, Y. Chen, and W. Duan, Nano Lett. **20**, 5400 (2020).

[23] B.-B. Fu, C.-J. Yi, T.-T. Zhang, M. Caputo, J.-Z. Ma, X. Gao, B. Lv, L.-Y. Kong, Y.-B. Huang, and P. Richard *et al.*, Sci. Adv. **5**, eaau6459 (2019).

[24] M. Xiao, L. Ye, C. Qiu, H. He, Z. Liu, and S. Fan, Sci. Adv. **6**, eaav2360 (2020).

[25] Y. Qie, J. Liu, S. Wang, Q. Sun, and P. Jena, J. Mater. Chem. A **7**, 5733 (2019).

[26] H. Xue, Y. Yang, and B. Zhang, Nat. Rev. Mater. **7**, 974 (2022).

[27] Q. Wei, X. Zhang, W. Deng, J. Lu, X. Huang, M. Yan, G. Chen, Z. Liu, and S. Jia, Nat. Mater. **20**, 812 (2021).

[28] H. Xue, Z. Wang, Y.-X. Huang, Z. Cheng, L. Yu, Y. X. Foo, Y. X. Zhao, S. A. Yang, and B. Zhang, Phys. Rev. Lett. **128**, 116802 (2022).

[29] C. He, H.-S. Lai, B. He, S.-Y. Yu, X. Xu, M.-H. Lu, and Y.-F. Chen, Nat. Commun. **11**, 2318 (2020).

[30] H. Wang, S. K. Gupta, B. Xie, and M. Lu, Front. Optoelectron. **13**, 50 (2020).

[31] Y. Liu, X. Chen, and Y. Xu, Adv. Funct. Mater. **30**, 1904784 (2020).

[32] Y. Liu, Y. Xu, and W. Duan, Research (Washington, D.C.) **2019**, 5173580 (2019).

[33] Y. Liu, Y. Xu, and W. Duan, Natl. Sci. Rev. **5**, 314 (2018).

[34] X. Wang, T. Yang, Z. Cheng, G. Surucu, J. Wang, F. Zhou, Z. Zhang, and G. Zhang, Appl. Phys. Rev. **9**, 041304 (2022).

[35] X. Chen, J. Liu, and J. Li, The Innovation **2**, 100134 (2021).

[36] J. Chen, J. He, D. Pan, X. Wang, N. Yang, J. Zhu, S. A. Yang, and G. Zhang, Sci. China Phys. Mech. Astron. **65**, 117002 (2022).

[37] T. Zhang, Z. Song, A. Alexandradinata, H. Weng, C. Fang, L. Lu, and Z. Fang, Phys. Rev. Lett. **120**, 016401 (2018).

[38] H. Miao, T. T. Zhang, L. Wang, D. Meyers, A. H. Said, Y. L. Wang, Y. G. Shi, H. M. Weng, Z. Fang, and M. P. M. Dean, Phys. Rev. Lett. **121**, 035302 (2018).

[39] Q.-B. Liu, Z. Wang, and H.-H. Fu, Phys. Rev. B **103**, L161303 (2021).

[40] R. Wang, B. W. Xia, Z. J. Chen, B. B. Zheng, Y. J. Zhao, and H. Xu, Phys. Rev. Lett. **124**, 105303 (2020).

[41] M. Zhong, Y. Han, J. Wang, Y. Liu, X. Wang, and G. Zhang, Phys. Rev. Mater. **6**, 084201 (2022).

[42] G. Ding, F. Zhou, Z. Zhang, Z.-M. Yu, and X. Wang, Phys. Rev. B **105**, 134303 (2022).

[43] J.-Y. You, X.-L. Sheng, and G. Su, Phys. Rev. B **103**, 165143 (2021).

[44] G. Liu, Z. Huang, Z. Chen, Y. Jin, C. He, and H. Xu, Phys. Rev. B **106**, 054306 (2022).

[45] S. Singh, Q. S. Wu, C. Yue, A. H. Romero, and A. A. Soluyanov, Phys. Rev. Mater. **2**, 114204 (2018).

[46] P. C. Sreeparvathy, C. Mondal, C. K. Barman, and A. Alam, Phys. Rev. B **106**, 085102 (2022).

[47] Y. Feng, C. Xie, H. Chen, Y. Liu, and X. Wang, Phys. Rev. B **106**, 134307 (2022).

[48] Z. J. Chen, R. Wang, B. W. Xia, B. B. Zheng, Y. J. Jin, Y.-J. Zhao, and H. Xu, Phys. Rev. Lett. **126**, 185301 (2021).

[49] C. Xie, Y. Liu, Z. Zhang, F. Zhou, T. Yang, M. Kuang, X. Wang, and G. Zhang, Phys. Rev. B **104**, 045148 (2021).

[50] T. Yang, C. Xie, H. Chen, X. Wang, and G. Zhang, Phys. Rev. B **105**, 094310 (2022).

[51] M. Zhong, Y. Liu, F. Zhou, M. Kuang, T. Yang, X. Wang, and G. Zhang, Phys. Rev. B **104**, 085118 (2021).

[52] J. Wang, H. Yuan, Y. Liu, F. Zhou, X. Wang, and G. Zhang, Phys. Chem. Chem. Phys. **24**, 2752 (2022).

[53] F. Zhou, Z. Zhang, H. Chen, M. Kuang, T. Yang, and X. Wang, Phys. Rev. B **104**, 174108 (2021).

[54] B. Zheng, B. Xia, R. Wang, Z. Chen, J. Zhao, Y. Zhao, and H. Xu, Phys. Rev. B **101**, 100303(R) (2020).

[55] G. Ding, T. Sun, and X. Wang, Phys. Chem. Chem. Phys. **24**, 11175 (2022).

[56] F. Zhou, H. Chen, Z.-M. Yu, Z. Zhang, and X. Wang, Phys. Rev. B **104**, 214310 (2021).

[57] Y. S. Chen, F. F. Huang, P. Zhou, Z. S. Ma, and L. Z. Sun, New J. Phys. **23**, 103043 (2021).

[58] J. Li, J. Liu, S. A. Baronett, M. Liu, L. Wang, R. Li, Y. Chen, D. Li, Q. Zhu, and X. Chen, Nat. Commun. **12**, 1204 (2020).

[59] J. H. Wang, H. K. Yuan, Z. M. Yu, Z. Y. Zhang, and X. T. Wang, Phys. Rev. Mater. **5**, 124203 (2021).

[60] Q.-B. Liu, H.-H. Fu, and R. Wu, Phys. Rev. B **104**, 045409 (2021).

[61] Q.-B. Liu, Z.-Q. Wang, and H.-H. Fu, Mater. Today Phys. **24**, 100694 (2022).

[62] M. Wang, Y. Wang, Z. Yang, J. Fan, B. Zheng, R. Wang, and X. Wu, Phys. Rev. B **105**, 174309 (2022).

[63] G. Liu, Y. Jin, Z. Chen, and H. Xu, Phys. Rev. B **104**, 024304 (2021).

[64] T. T. Zhang, H. Miao, Q. Wang, J. Q. Lin, Y. Cao, G. Fabbris, A. H. Said, X. Liu, H. C. Lei, Z. Fang, H. M. Weng, and M. P. M. Dean, Phys. Rev. Lett. **123**, 245302 (2019).

[65] Q.-B. Liu, Z.-Q. Wang, and H.-H. Fu, Phys. Rev. B **104**, L041405 (2021).

[66] C. Xie, H. Yuan, Y. Liu, and X. Wang, Phys. Rev. B **105**, 054307 (2022).

[67] C. Xie, H. Yuan, Y. Liu, X. Wang, and G. Zhang, Phys. Rev. B **104**, 134303 (2021).

[68] H.-D. Saßnick and C. Cocchi, J. Chem. Phys. **156**, 104108 (2022).

[69] T.-N. Pham Thi, J.-C. Dumas, V. Bouineau, N. Dupin, C. Guéneau, S. Gosse, P. Benigni, P. Maugis, and J. Rogez, Calphad **48**, 1 (2015).

[70] R. G. Parr, Annu. Rev. Phys. Chem. **34**, 631 (1983).

[71] J. Hafner, J. Comput. Chem. **29**, 2044 (2008).

[72] J. P. Perdew, K. Burke, and M. Ernzerhof, Phys. Rev. Lett. **80**, 891 (1998).

[73] P. E. Blöchl, Phys. Rev. B **50**, 17953 (1994).
[74] A. Togo and I. Tanaka, Scr. Mater. **108**, 1 (2015).
[75] Q.-S. Wu, S.-N. Zhang, H.-F. Song, M. Troyer, and A. A. Soluyanov, Comput. Phys. Commun. **224**, 405 (2018).
[76] M. P. L. Sancho, J. M. L. Sancho, and J. Rubio, J. Phys. F: Met. Phys. **15**, 851 (1985).
[77] https://oqmd.org/materials.
[78] See Supplemental Material at http://link.aps.org/supplemental/10.1103/PhysRevB.107.024304 for the band structures for the eight Cs-Te systems and the phonon dispersion for the C2/m-Cs_5Te_3 primitive cell.
[79] K. Maeda, S. Sasaki, M. Kato, and Y. Kihara, J. Nucl. Mater. **385**, 178 (2009).
[80] H. Nielsen and M. Ninomiya, Nucl. Phys. B **185**, 20 (1981).
[81] H. Nielsen and M. Ninomiya, Nucl. Phys. B **193**, 173 (1981).
[82] R. de Boer and E. Cordfunke, J. Alloys Compd. **228**, 75 (1995).
[83] G. Prins and E. Cordfunke, J. Less-Common Met. **104**, L1 (1984).
[84] P. Böuttcher and U. Kretschmann, Z. Anorg. Allg. Chem. **491**, 39 (1982).
[85] P. Böttcher, J. Less-Common Met. **70**, 263 (1980).
[86] P. Böttcher and U. Kretschmann, Z. Anorg. Allg. Chem. **523**, 145 (1985).
[87] E. Burkel, Rep. Prog. Phys. **63**, 171 (2000).
[88] W. M. Shaw and L. D. Muhlestein, Phys. Rev. B **4**, 969 (1971).
[89] H. Lourenço-Martins and M. Kociak, Phys. Rev. X **7**, 041059 (2017).
[90] G. Benedek and J. P. Toennies, Surf. Sci. **299-300**, 587 (1994).
[91] A. Bera, S. Bera, S. Kalimuddin, S. Gayen, M. Kundu, B. Das, and M. Mondal, Eur. Phys. J. Spec. Top. **230**, 4113 (2021).
[92] J. Zhu, W. Wu, J. Zhao, H. Chen, L. Zhang, and S. A. Yang, npj Quantum Mater. **7**, 52 (2022).